

Star-Image Centering with Deep Learning II: HST/WFPC2 Full Field of View

DANA I. CASSETTI-DINESCU,^{1,2} ROBERTO BAENA-GALLÉ,³ TERENCE M. GIRARD,¹ ALEJANDRO CERVANTES-ROVIRA,³ AND SEBASTIAN TODEASA^{4,1}

¹*Department of Physics, Southern Connecticut State University, 501 Crescent Street, New Haven, CT 06515*

²*Astronomical Institute of the Romanian Academy, Cutitul de Argint 5, Sector 4, Bucharest, Romania*

³*Universidad Internacional de la Rioja, Avenida de la Paz, 137,26006, Logroño, La Rioja, Spain*

⁴*Physics, Applied Physics and Astronomy Department, Rensselaer Polytechnic Institute, 110 8th Street, Troy, NY 12180*

Submitted to PASP

ABSTRACT

We present an expanded and improved deep-learning (DL) methodology for determining centers of star images on HST/WFPC2 exposures. Previously, we demonstrated that our DL model can eliminate the pixel-phase bias otherwise present in these undersampled images; however that analysis was limited to the central portion of each detector.

In the current work we introduce the inclusion of global positions to account for the PSF variation across the entire chip and instrumental magnitudes to account for nonlinear effects such as charge transfer efficiency. The DL model is trained using a unique series of WFPC2 observations of globular cluster 47 Tuc, data sets comprising over 600 dithered exposures taken in each of two filters — F555W and F814W.

It is found that the PSF variations across each chip correspond to corrections of the order of ~ 100 mpix, while magnitude effects are at a level of ~ 10 mpix. Importantly, pixel-phase bias is eliminated with the DL model; whereas, with a classic centering algorithm, the amplitude of this bias can be up to ~ 40 mpix. Our improved DL model yields star-image centers with uncertainties of 8-10 mpix across the full field of view of WFPC2.

Keywords: Astrometry: Space astrometry — Neural networks: Convolutional neural networks

1. INTRODUCTION

The astrometric potential, for proper-motion purposes, is yet to be fully realized for archival images taken with the Wide-Field Planetary Camera 2 (WFPC2), a legacy instrument of the Hubble Space Telescope (HST). Recently we have developed a deep-learning (DL) methodology to improve the centering precision of images taken with WFPC2. These images are severely undersampled and thus suffer from a fractional pixel bias in the stars' centers due to the mismatch between the true PSF and the PSF used by the centering algorithm. To address this problem, Anderson & King (2000) built an *effective* PSF (ePSF) empirically from a set of observations. However, the WFPC2 ePSF library is not

sufficient to remove this pixel-phase bias which can be as large as 40 to 50 mpix. Once post corrections such as the 34th-row correction (Anderson & King 1999) and classic distortion (Anderson & King 2003) are applied, the pixel-phase bias is manifested as unaccounted-for noise in the positions. As a consequence, WFPC2 was deemed unfit for high-precision astrometry and a large archive with images taken between 1993 and 2009 remains untapped for proper-motion studies.

Taking an entirely new approach to determining stellar centers in WFPC2 images, we developed and refined a DL code using both simulated and real data as described in Baena-Gallé et al. (2023) and in Casetti-Dinescu et al. (2023, hereafter, Paper I). At that time, we focused only on the central part of each WFPC2 chip to avoid the complexity of the PSF variation across the detector's field of view. We modeled filters F555W and F814W thanks to a unique data set available only in these two filters. The method proved successful, yield-

ing centering uncertainties of the order of 10 mpix per single measurement near the center of each chip.

In the current work, we have expanded upon our previous model and restructure the DL code to include the variation of the PSF across the chip as well as magnitude effects in the determination of new stellar centers. In what follows, we will make frequent reference to Paper I and encourage the interested reader to look there for additional, specific details.

2. DEEP LEARNING MODEL

2.1. Model Input

The data sets we use to build the DL model were taken in July 1999 at the core of globular cluster 47 Tuc (PID 8267, Gilliland). These data are unique as there are over 600 exposures in each filter, taken with fractional-pixel offsets in each axis, ranging up to about 2 PC pixels (0.046 "/pixel). These offsets are critical in characterizing the pixel-phase bias. Conveniently, on the scale of these offsets, effects due to differential optical distortion and the 34th-row error can effectively be ignored. The pattern of offsets is shown in Figure 1 of Paper I; there is good coverage in both x and y chip coordinates. There are 636 exposures in F555W and 654 in F814W, all having 160 seconds per exposure. The data set is time-wise contiguous, taken over some 8 days of observations.

We begin by first centering all exposures with the classic ePSF-algorithm `hst1pass`¹ code (Anderson & King 2000; Anderson 2022). It is worth noting that this code employs a library consisting of a spatial grid of PSFs, meant to properly model its variability across each chip. As in Paper I, the `hst1pass`-determined positions are used to construct an average catalog in each filter. This is done by transforming the positions of each exposure into those of one chosen as reference (typically the first one in the set). In this way we obtain positions on the same system for all exposures, which are afterwards averaged with outlier clipping. The polynomial transformations between target and reference exposures include up to third-order terms. From this average catalog we eliminate all objects that have a neighbor within 5 pixels, in order that crowding effects do not affect the training of the DL model. The average catalog positions are then used as “true” positions in the training process. The assumption is that these catalog positions are no longer affected by pixel-phase bias given the large number of nearly-random offsets being averaged over.

¹ While using a 2019 version of the code, we have checked that the 2022 version (Anderson 2022) gives the same results for WFPC2 images; the ePSF library is identical in the two versions of the code.

Table 1. Number of input objects per chip and filter

Filter	N_{exp}	N_{PC}	N_{WF2}	N_{WF3}	N_{WF4}
F555W	636	2073996	1848851	2118360	1949340
F814W	654	2378226	2290724	2524498	2371043

Specifically, the input for the training process consists of the intensity values of a raster of 6×6 pixels centered on each star image, along with the star’s catalog-determined (x, y) center with respect to the bottom left corner of the raster. In addition, we also input the global X, Y coordinates of the raster within the chip, and the star’s instrumental magnitude. The global-coordinate input will allow the model to compensate for the variation of the PSF across the field of view, while the input magnitudes provide allowance for what we suspect may also be a slight magnitude dependence present in the PSF. Just to be clear, no attempt is made to have the model predict stellar magnitudes; we are entirely focused on determining image centers.

The number of input objects per chip and filter are listed in Table 1. Compared to Paper 1, we have a factor of ~ 9 more objects, as in that paper we modeled only the central 1/3 of the chip.

2.2. Model Description

Our specific Convolutional Neural Network (CNN) model is developed from that presented in Baena-Gallé et al. (2023) and Paper I. There, the DL model is based on the VGG architecture (Simonyan & Zisserman 2014). Our approach does not make any assumption regarding PSF shape, which is fundamentally different from classic centering methods. Instead, the (x, y) coordinates of stellar centers are estimated by measuring correlations with pixel intensity values within a 6×6 square raster around each star.

The new architecture is illustrated in Figure 1. The model consists of eight trainable layers, six of them convolutional and the last two fully-connected (FC) layers, with two outputs that provide paired estimates along the x - and y -axis, respectively. Hence, it should be considered a VGG8 model. One maxpool layer is inserted every two convolutional ones, and all hidden layers are equipped with Rectified Linear Unit (*ReLU*) non-linear activation functions except the last one, which is *linear*, in accordance with the regression nature of this problem. As in Paper I, inserting a batch-normalization layer after the fourth convolutional one helps stabilize the convergence process in our specific problem.

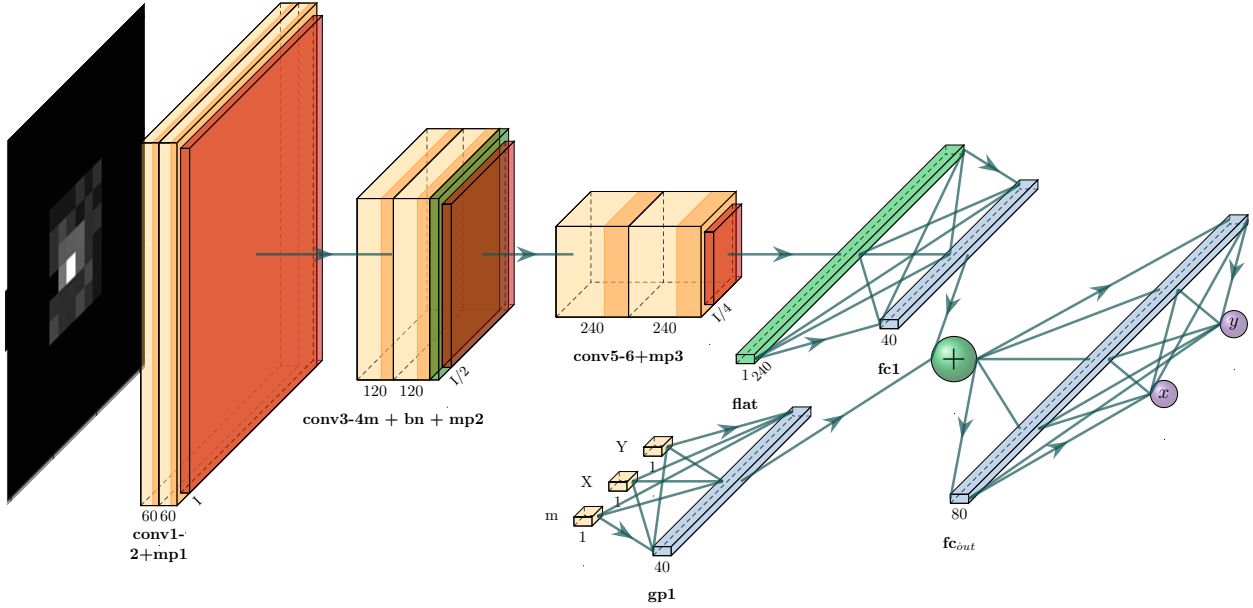


Figure 1. VGG8 model architecture. Input scalars are magnitude (m) and absolute position (X, Y). Outputs are x and y .

Table 2. VGG model

Layer (type)	Output shape	# of param.	Connected to
conv1_input (InputLayer)	(None, 12, 12, 1)	0	[]
conv1 (Conv2D)	(None, 12, 12, 60)	1560	['conv1_input[0][0]']
conv2 (Conv2D)	(None, 12, 12, 60)	90060	['conv1[0][0]']
max_pooling2d (MaxPooling2D)	(None, 6, 6, 60)	0	['conv2[0][0]']
conv3 (Conv2D)	(None, 6, 6, 120)	180120	['max_pooling2d[0][0]']
conv4 (Conv2D)	(None, 6, 6, 120)	360120	['conv3[0][0]']
bn_2 (BatchNormalization)	(None, 6, 6, 120)	480	['conv4[0][0]']
max_pooling2d_1 (MaxPooling2D)	(None, 3, 3, 120)	0	['bn_2[0][0]']
conv5 (Conv2D)	(None, 3, 3, 240)	259440	['max_pooling2d_1[0][0]']
conv6 (Conv2D)	(None, 3, 3, 240)	518640	['conv5[0][0]']
max_pooling2d_2 (MaxPooling2D)	(None, 1, 1, 240)	0	['conv6[0][0]']
flatten (Flatten)	(None, 240)	0	['max_pooling2d_2[0][0]']
gp_1_input (InputLayer)	(None, 3)	0	[]
fc_1 (Dense)	(None, 40)	9640	['flatten[0][0]']
gp_1 (Dense)	(None, 40)	160	['gp_1_input[0][0]']
concatenate (Concatenate)	(None, 80)	0	['fc_1[0][0]', 'gp_1[0][0]']
fc_out (Dense)	(None, 2)	162	['concatenate[0][0]']
Total parameters 1420382; trainable parameters 1420142			

As an important novelty with respect to Paper I, scalar parameters, such as the star magnitude m and its global position within the CCD (X and Y), are fed into an FC layer and then concatenated to the features extracted along the main branch before the last fully connected layer. The underlying idea is that the main branch computes estimates based on correlations between the intensity values within the raster, while the scalar parameters perform a fine tuning informing the network about possible dependencies of the PSF shape with respect to the star magnitude and its position across the CCD.

The design process of the model also differs with respect to the aforementioned VGG6 model in Paper I in two important aspects. Firstly, in Paper I the architecture and the hyperparameter space values (i.e., number of layers and kernels within, kernels sizes, number of batches and epochs, type of optimizer, loss function, etc.) were derived from a set of ~ 4000 mock stars in each chip. The model was then trained over a data set of real stars in WFPC2 images. Therefore, although the simulator used to create the mock images was based on the WFPC2 ePSF library of Anderson & King (2000), one may expect an inconsistency between the dataset used to design the hyperparameter space of the model and the dataset used to train, validate and test it. In the current work, for the sake of consistency of the model at both design and training stages, we used real star images throughout. Specifically, at the design stage we used a subset of ~ 12000 star images (from the F555W PC chip).

Secondly, we have performed an automatic search across the hyperparameter space of solutions to find the best combination. For this purpose, the *HalvingRandomSearchCV* estimator was used, which searches within a parameter space using successive halving (Li et al. 2016). This is somewhat like a competition between different candidate combinations. It is an iterative selection process where all candidates — i.e., the hyperparameter combinations — are evaluated using a small amount of resources in the first iteration. Those combinations considered the best are selected for the next iteration, which are then allocated more resources. Hence, the number of resources are increased as the number of candidates decreases until finding the best combination of hyperparameters. Other estimators make use of grid parameter search strategies, which are more exhaustive but more expensive in terms of computational burden.

After exploring several hundreds of hyperparameter combinations with this tool, we found our best design with the following hyperparameters: 6 convolutional layers, 60 kernels in the first group of two, doubling the

number of kernels as the model increases in depth. Both the flattened output of the convolutional part and the three scalar inputs are processed by FC layers of 40 neurons, concatenated and passed to the output FC layer of 80 neurons. Thus, the network has a total of $\sim 1.4M$ trainable parameters. The properties of the model are shown in Table 2 and in Figure 1. The same architecture is used for all four WFPC2 chips and both filters.

For comparison, the VGG6 model in Paper I was made up of $\sim 0.2M$ trainable parameters. The difference between that model and the new VGG8 illustrates the increase in complexity. The new model must account for the variation of the PSF across the chip, as well as the variation of the PSF with magnitude.

We also obtained a best learning rate of 4×10^{-5} , and a weight decay 8×10^{-3} . Different loss functions and metrics for validation were tried, such as the *logcosh*, *huber_loss*, or *cosine_similarity*, and the *MeanAbsoluteError*. The last of these was found to be the most efficient (as in Paper I). Finally, different types of optimizer were also tested such as *Adam*, *Nadam*, or *RMSProp*. We found *AdamW* provided the best solution with an Exponential Moving Average (EMA) momentum equal to 0.95. The input data set of stars was divided into subgroups of 70 : 10 : 20% for training, validation, and final testing, respectively. We did not find noticeable differences with respect to the batch size. All input cutout images' intensities are first normalized to a sum of one. The initial 6×6 raster images are zero-padded, thus increasing their size to 12×12 . This guarantees the relevant information (i.e., pixel intensities) within the raster is preserved as the network layers reduce their sizes due to edge effects after convolutions with the kernels. The model was designed in Keras/TF (Chollet & others 2018).

2.3. Model Outcome

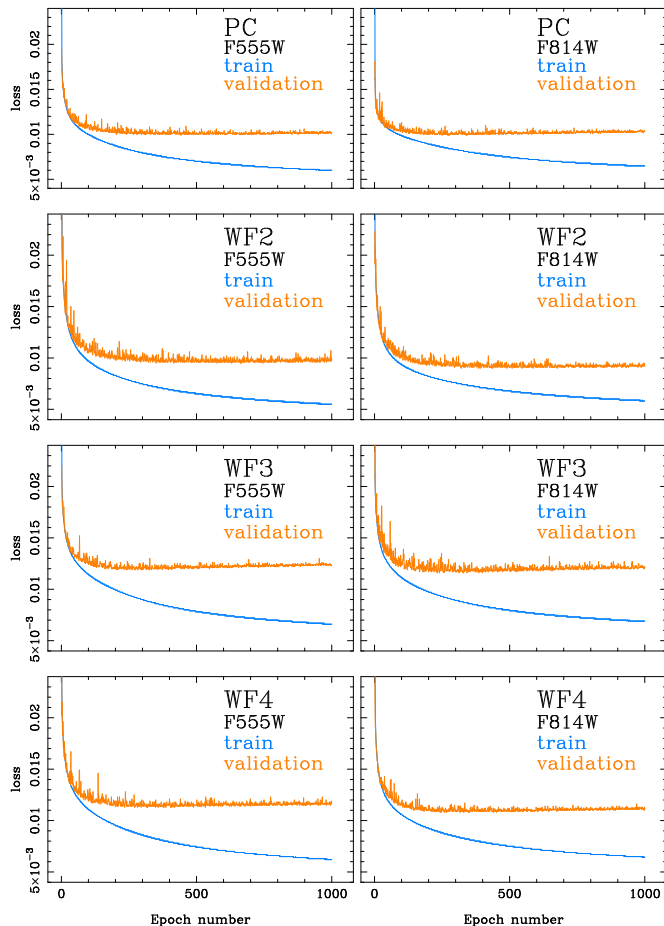
In Figure 2 we show the loss function for the training (70%) and the validation (10%) samples as a function of epoch during the training process. We have experimented with a couple of values for the number of epochs, and eventually settled for 1000. The curves indicate that no overfitting is present.

Next, we look at the test sample which consists of 20% of the input objects listed in Tab. 1. We calculate the standard deviation of the differences between output and input positions for the test sample and list these in Table 3. To calculate these standard deviations, we limit the test sample to a magnitude range corresponding to well measured stars, which is the same for all chips and filters. We also discard 3σ outliers. The values in Tab. 3 represent the centering error per single measurement

Table 3. Standard deviations of position differences and number of objects in each test sample

Chip	F555W			F814W		
	σ_x	σ_y	N_{obj}	σ_x	σ_y	N_{obj}
PC	8.6	9.1	367955	9.2	9.6	427849
WF2	9.0	8.9	233466	7.8	7.7	395907
WF3	8.7	8.7	331569	9.2	9.0	404576
WF4	8.2	8.6	312578	8.3	8.7	388009

in detector millipixels (0.046 "/pixel for the PC and 0.10 "/pixel for WF chips). Note these are conservative estimates, as they assume the input catalog positions are completely free of error.

**Figure 2.** The loss function trend with epoch for the four chips and the two filters. Training and validation samples are shown.

3. APPLYING THE DL MODEL

3.1. Cluster Results

The models derived in Sec. 2 are now applied to the (hst1pass-determined) detections in all exposures of the NGC 104 data set, as well as to other cluster data sets that have not participated in the building of the model. We require data sets that are rich in well-measured stars and have repeated exposures with small offsets, such that other possible systematic errors operating on scales of tens of pixels do not affect the analysis.

We use the same cluster data sets as in Paper I, as these have already been deemed the most appropriate for such testing. The cluster fields, per filter, are listed in Table 4, including the number of exposures, exposure times, and the epoch of observation. In the last column of Tab 4 we add a data set number that corresponds to the specific MAST DOI link listed in the Acknowledgments.

Star detection and cutout rasters are made using hst1pass star centers as preliminary position estimates. Then, the DL models, by filter and chip, are applied to each of these sets to calculate new star centers.

To evaluate these, polynomial transformations of star positions are made for each exposure into a chosen reference exposure and the standard errors of these transformations are recorded. The standard errors are then plotted as a function of the pixel phase of the offset from the reference exposure. We denote this pixel phase of the offset ϕ , and its value ranges from 0 to 1. In other words, this is the fractional part of the full offset. In such plots, the pixel-phase bias shows itself as a curve with minimum standard error at $\phi = 0$ and 1, but rising to an elevated level at mid values of ϕ . Conversely, when no pixel-phase bias is present, the standard error curves will be flat. The entire process is repeated using the original hst1pass centers, in order to compare the amount of pixel-phase bias present in the two centering algorithms.

The results for NGC 104 in F555W presented in Figure 3 show a dramatic improvement of the DL positions over those obtained with hst1pass, in all four chips. This demonstrates that the method works, not only for the central part of the chip as shown in Paper I, but also across the full field of view of each chip. Our refinement of the DL model has effectively allowed for modeling of the PSF variation across the chip.

Results for the other data sets observed in filter F555W are shown in Figures 4, 5 and 6.

Note that the DL models applied to these sets were trained on (70% of) the NGC 104 data, while the target sets were taken at a different observation epoch, at which temporal changes in the PSF may become important. Also, none of these sets match the number of repeats

Table 4. Data sets used to test the DL models

Target field	N_{exp}	Exp. time	Epoch	Data Set #
F555W				
NGC 104	636	160	1999.5	1
NGC 6752 - PC	118	26	1994.6	3
NGC 6441	36	160	2007.3	4
NGC 6341	28	100	2008.1	5
F814W				
NGC 104	653	160	1999.5	2
NGC 6752 - PC	109	50	1994.6	6
NGC 6656	162	260	1999.1	7
NGC 6205	25	140	1999.8	8
NGC 5139	24	80	2008.1	9

and offset-phase ϕ coverage of the NGC 104’s data sets. Therefore, the standard error plots appear less coherent. Lastly, variation in the observation exposure times and richness of these other target clusters yield a large range in quality for their standard-error plots.

The data set for NGC 6752 had only PC observations, in both filters. In spite of the poor sampling in offset pixel phase, the trends are apparent: the DL positions are less affected by the bias error compared to the *hst1pass* positions — see Figs 4 and 8.

Results for clusters NGC 6441 and NGC 6341 shown in Figures 5 and 6 show great improvement for the PC, but more modest improvement for the WF chips. Since these observations are taken some 8 to 9 years after the NGC 104 set, it is possible that the PSF of the WF chips varied with time, and thus the NGC 104-based model is less representative for these two clusters.

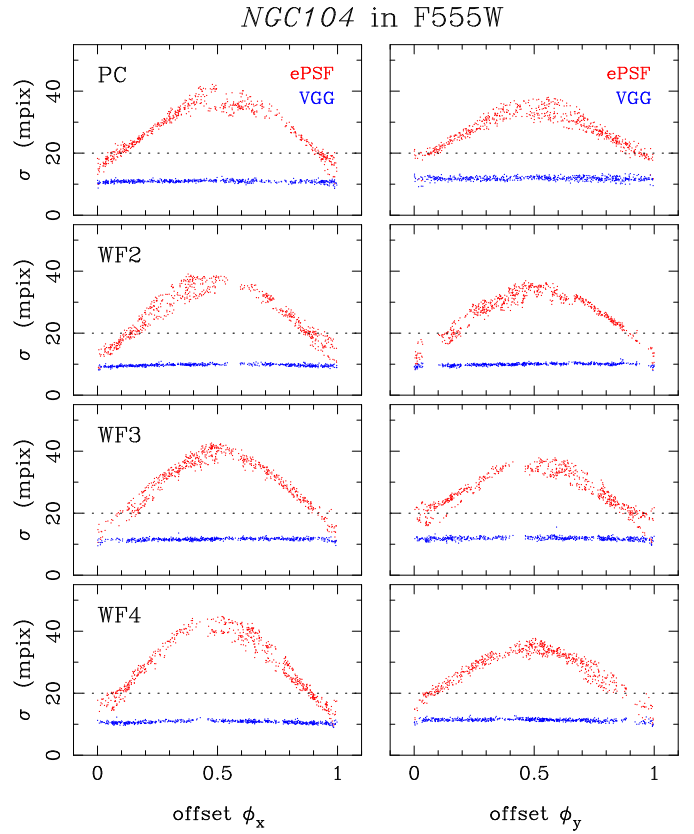


Figure 3. Standard error of the transformation (of a target exposure into the reference exposure) as a function of offset phase. Each row represents a chip while x - and y -coordinate values are shown in the left and right panels, respectively. Larger standard errors near mid-pixel phase indicate the presence of pixel-phase bias in the positions. The classic ePSF/*hst1pass* centering algorithm is shown with red symbols, while the DL algorithm is shown with blue symbols. A benchmark level of 20 mpix is shown with a dotted line. Note the flat curves obtained for the DL centers at ~ 10 mpix. These results are for exposures of NGC 104 in filter F555W.

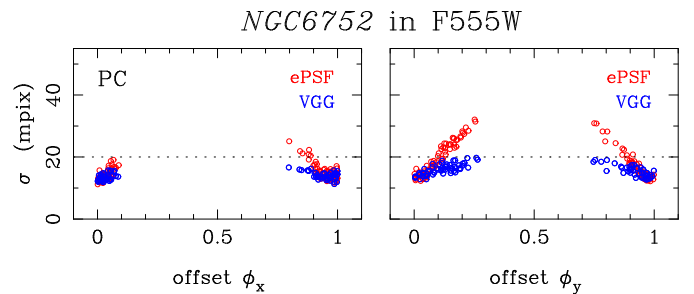
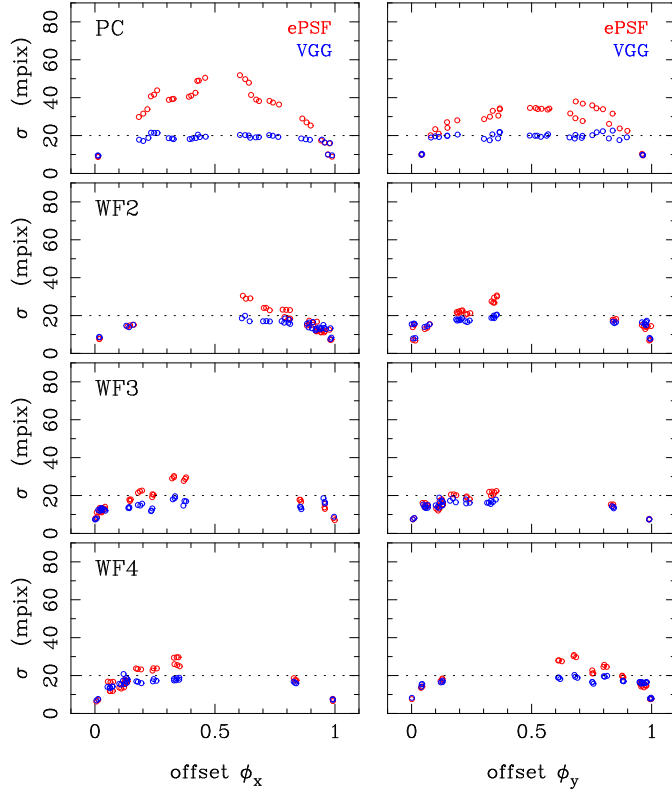
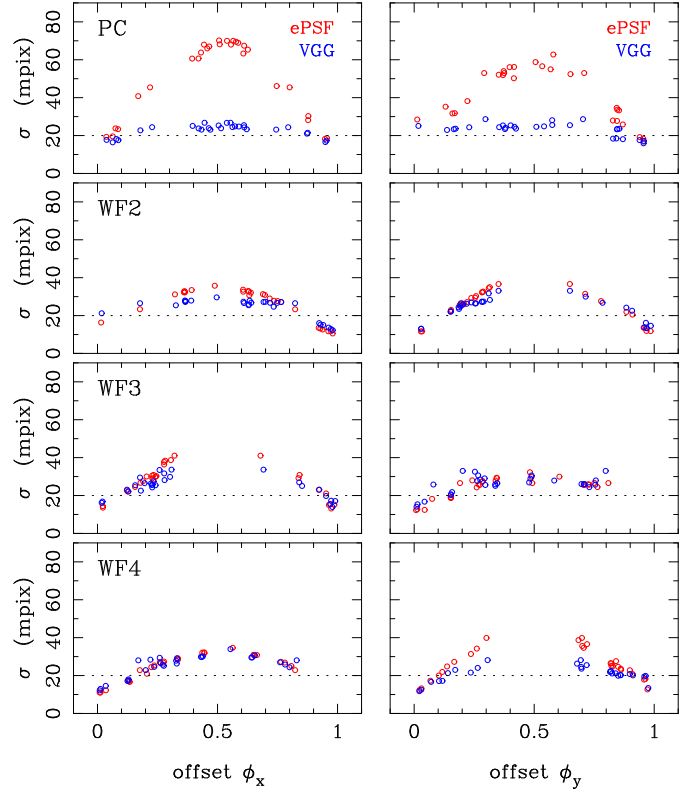


Figure 4. As in Fig. 3, only for NGC 6752 in F555W. The phase coverage is poor in this case, however the trends of the curves are apparent.

NGC6441 in F555W**Figure 5.** As in Fig. 3, only for NGC 6441 in F555W.

In filter F814W, the NGC 104 results once again show great improvement in removing the pixel-phase bias (see Figure 7). Results for NGC 6656 and NGC 6205 shown in Figures 9 and 10 are good for the WF chips and more modest for the PC. Finally, for cluster NGC 5139 there is hardly any improvement of the DL positions over the *hst1pass* ones as seen in Figure 11. Overall, this data set has large errors, in excess of 20 mpix, and the curves are rather flat, hardly indicating a pixel-phase bias. It is possible that the signal-to-noise ratio dominates the errors in this case. Therefore, we regard this data set as less instructive in assessing the DL model versus the *hst1pass* one, but include it for the sake of completeness, as it was also presented in Paper I.

NGC6341 in F555W**Figure 6.** As in Fig. 3, only for NGC 6341 in F555W. This data set is the farthest in time with respect to the NGC 104 set on which the DL model is trained. Therefore, long-term time variation of the PSF may be responsible for the lesser improvement of image centers in the WF chips.

NGC104 in F814W

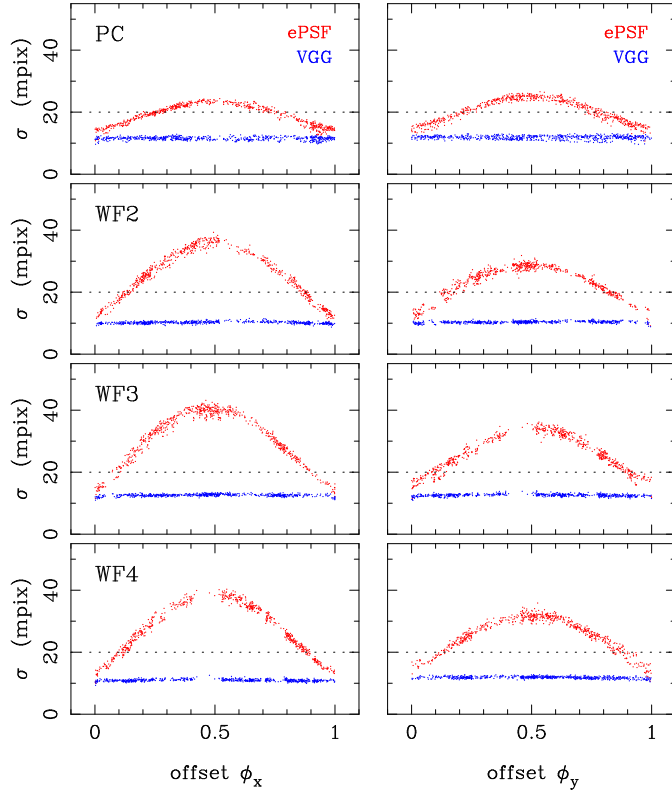


Figure 7. As in Fig. 3, only for NGC 104 in F814W.

NGC6656 in F814W

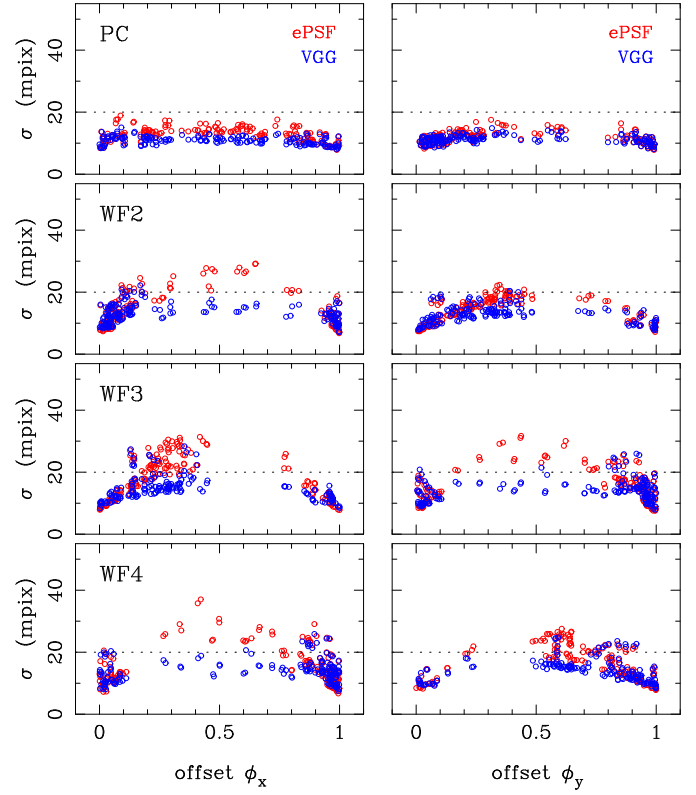


Figure 9. As in Fig. 3, only for NGC 6656 in F814W.

NGC6752 in F814W

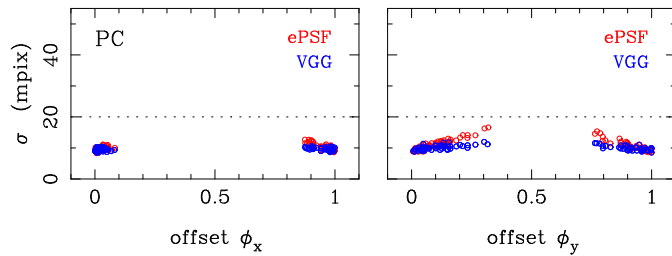
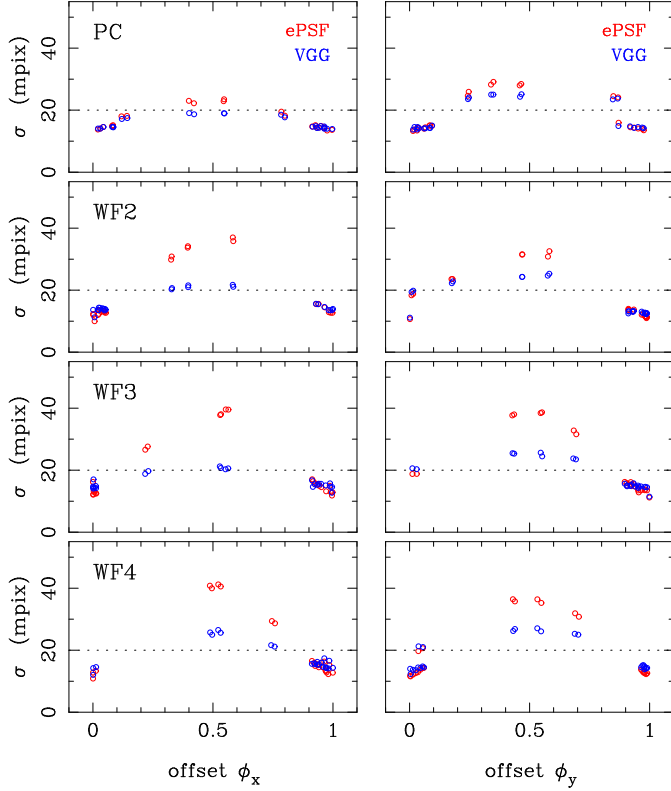
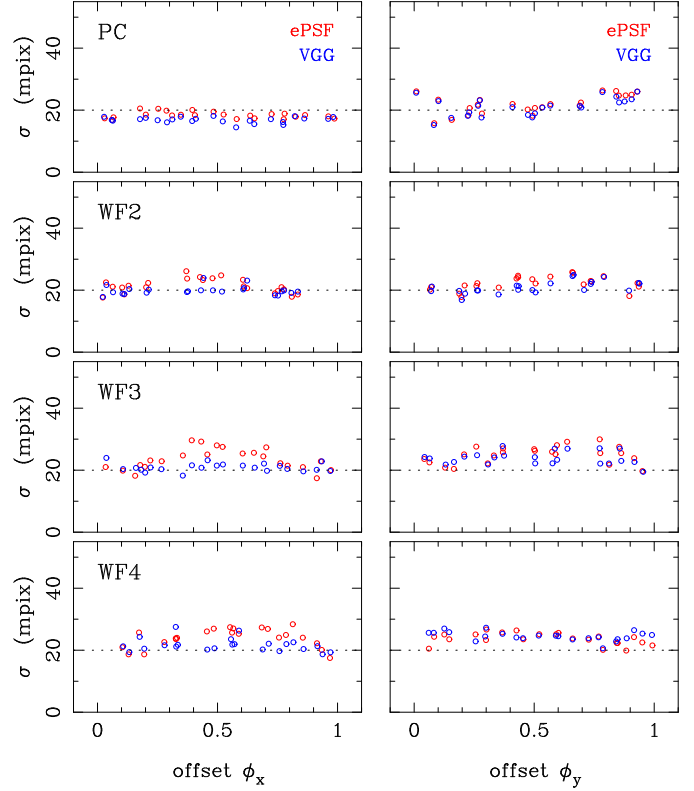


Figure 8. As in Fig. 3, only for NGC 6752 in F814W.

NGC6205 in F814W

**Figure 10.** As in Fig. 3, only for NGC 6205 in F814W.

NGC5139 in F814W

**Figure 11.** As in Fig. 3, only for NGC 5139 in F814W.

3.2. Characterizing the Impact of Global Positions and Magnitude

One of the main modifications made to our DL model, over that presented in Paper I, is the inclusion of layers making use of the star’s rough global position and instrumental magnitude. The expectation is that these would effectively model the known variation of the PSF across the chip and any possible dependence on magnitude. How important are these new parameters in the derived DL model solutions?

As a trained DL model solution can very much be a ‘black box’ in some respect, a simple test was performed to measure the sensitivity of the model output to these specific input parameters. A single star image was chosen from an exposure in the NGC 104 data set, more precisely, one star near the center of each chip for a single F555W exposure and a single F814W exposure. The star images were selected to be relatively bright, that is, with high signal to noise. The DL model solution, appropriate to that chip and filter, was applied to the star’s image, using its actual intensity raster cutout and correct global position and instrumental magnitude. Additionally, artificial repeats of the same image raster cutout were made placing it at a grid of positions across

the chip, while keeping the input magnitude correct. Finally, repeats were also made at the correct, near-center position, but with a range of input magnitudes, spanning the effective range of magnitudes used to train the model, i.e., the range over which the model solution should be legitimate.

The changes in the DL-calculated output centers, as a function of global position and magnitude, will measure the dependence of the centers on those input parameters. The calculated center at the actual position and magnitude is used as fiducial and differences are taken with the centers derived while varying the global position and magnitude, taking into account the additional integer-value offsets for the grid of global positions.

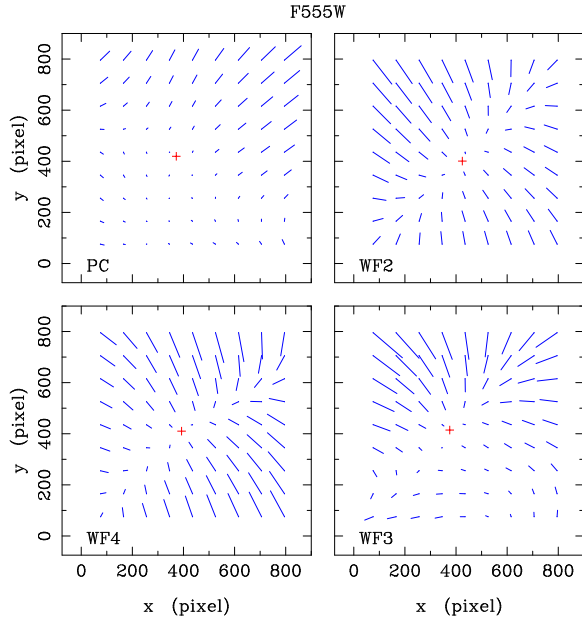


Figure 12. Sensitivity of the trained DL models to location on the chip, for an F555W exposure. At each 2-d grid point, the vector shows the amount of change in model-calculated x and y star-image position had this centrally located star’s image actually been at the indicated location on the chip. The vectors are magnified by a factor of 1000. The length of the longest vector shown is roughly 160 mpix. The plus symbol indicates the actual location of the star image on the chip. The four WFPC2 chips are as labeled.

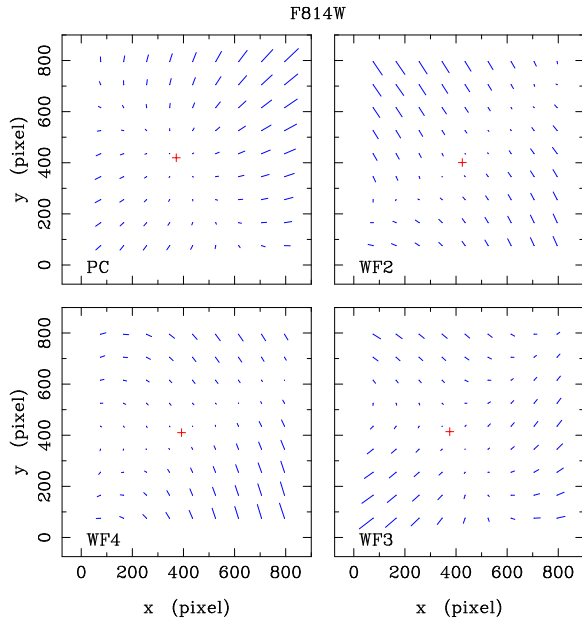


Figure 13. The same as Fig 12 but for a filter F814W exposure.

Figures 12 and 13 show the sensitivity of the calculated positions to the location of the image on the chip.

The vectors indicate the change in calculated image center relative to what would have been determined had the image been at its true location near the center of the chip. The length of the largest vectors in these figures is roughly 160 mpix, although near the edges of the chip, the changes are more typically of the order of ~ 50 mpix. This demonstrates a rather large dependence on global position, considering the ~ 10 mpix precision of the centers. In other words, the PSF does vary significantly across the chip and yet the model solution is able to make these large adjustments with precision. Note that the variation, especially for the WF chips, is much greater for the F555W filter than in F814W.

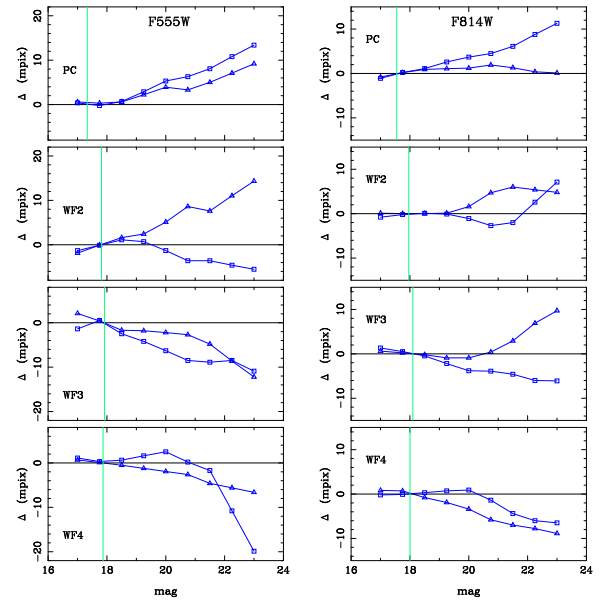


Figure 14. Sensitivity of the trained DL model to input magnitude. Differences in model-calculated centers are shown as a function of input magnitude. In each panel, square symbols show changes along the x axis, while triangles show the y -axis changes. The vertical line indicates the actual instrumental magnitude of the star image. Filter and WFPC2 chip are as labeled.

In Figure 14, the dependence on magnitude is shown. Within each panel, the two curves illustrate the changes along the x and y axes, while the vertical line indicates the actual instrumental magnitude of this star’s image. Overall, the dependence on magnitude is of smaller amplitude and is less well-behaved, compared to the variation with global position. Still, the effect of varying the input magnitude over a 6-magnitude range results in a change in the calculated position of from 10 to 20 mpix. The sensitivity of the trained DL model to global position is quite large, while the effect due to magnitude is smaller but not negligible.

4. SUMMARY

We present a DL methodology that provides improved astrometric centering for the full field of view of the WFPC2, largely by overcoming the pixel-phase bias present in these undersampled images. This bias can be as large as 40 mpix when classic centering algorithms are used, presumably due to a mismatch between an algorithm’s fitting PSF and the actual PSF. The procedure we develop relies on a stellar-rich set of repeated exposures that have small offsets, well-sampled in fractional pixel phase, for the purpose of training a supervised DL model.

Our new results indicate errors of the order of 8 to 10 mpix in the centers of well-measured stars. We also found that the PSF variations across each chip correspond to corrections of the order of ~ 100 mpix, while magnitude effects are at a level of ~ 10 mpix.

While this procedure was developed specifically for undersampled WFPC2 images, preliminary testing has shown us that ACS/WFC exposures in narrow filters (e.g., F502N) also are affected by pixel-phase bias when using classic centering techniques. Thus, it may very well be possible to improve ACS/WFC star centering with a similar DL approach. Our goal is to explore this possibility in the future.

ACKNOWLEDGMENTS

This work was supported in part by the NASA Connecticut Space Grant Consortium faculty research grant 80NSSC20M0129, and by program HST-AR-15632 provided by NASA through a grant from the Space Telescope Science Institute, which is operated by the Association of Universities for Research in Astronomy, Inc.

RBG and ACR are funded by the research Project “ADELA: Aplicaciones de Deep Learning para Astrofísica”, with reference PP-2022-13, awarded by the Call “Proyectos Propios de Investigación UNIR 2022”. RBG acknowledges the Call for Grants for Research Stays Abroad 2022/2023 from UNIR, and the Call “Estancias de movilidad en el extranjero José Castillejo para jóvenes doctores”, with ref. CAS22/00094, from the Spanish Ministry for Universities.

All the *HST* data sets used in this paper can be found in MAST. The data set number is that from the last column of Table 4 as follows:

Set 1: <http://dx.doi.org/10.17909/n9b8-3721>
 Set 2: <http://dx.doi.org/10.17909/n07m-jb63>
 Set 3: <http://dx.doi.org/10.17909/q64r-dn92>
 Set 4: <http://dx.doi.org/10.17909/0d26-v967>
 Set 5: <http://dx.doi.org/10.17909/mk0b-mx64>
 Set 6: <http://dx.doi.org/10.17909/rhae-wf34>
 Set 7: <http://dx.doi.org/10.17909/mzj9-0y54>
 Set 8: <http://dx.doi.org/10.17909/h7dk-6j75>
 Set 9: <http://dx.doi.org/10.17909/9jm2-cf66>

Facilities: *HST* (WFPC2), MAST

REFERENCES

- Anderson, J. 2022, One-Pass HST Photometry with hst1pass, Instrument Science Report ACS 2022-02, ,
- Anderson, J., & King, I. R. 1999, *PASP*, 111, 1095
- . 2000, *PASP*, 112, 1360
- . 2003, *PASP*, 115, 113
- Baena-Gallé, R., Girard, T. M., Casetti-Dinescu, D. I., & Martone, M. 2023, in *Highlights on Spanish Astrophysics XI*, 312
- Casetti-Dinescu, D. I., Girard, T. M., Baena-Gallé, R., Martone, M., & Schwendemann, K. 2023, *PASP*, 135, 054501
- Chollet, F., & others. 2018, Keras: The Python Deep Learning library, Astrophysics Source Code Library, record ascl:1806.022, , , ascl:1806.022
- Li, L., Jamieson, K., DeSalvo, G., Rostamizadeh, A., & Talwalkar, A. 2016, arXiv e-prints, arXiv:1603.06560
- Simonyan, K., & Zisserman, A. 2014, arXiv e-prints, arXiv:1409.1556